The Astrophysical Journal, 793:88 (11pp), 2014 October 1 doi:10.1088/0004-637X/793/2/88

A BROADBAND X-RAY STUDY OF THE GEMINGA PULSAR WITH *NuSTAR* AND *XMM-NEWTON*

Kaya Mori[1], Eric V. Gotthelf[1], Francois Dufour[2], Victoria M. Kaspi[2], Jules P. Halpern[1], Andrei M. Beloborodov[1], Hongjun An[2], Matteo Bachetti[3,4], Steven E. Boggs[5], Finn E. Christensen[6], William W. Craig[5], Charles J. Hailey[1], Fiona A. Harrison[7], Chryssa Kouveliotou[8], Michael J. Pivovaroff[9], Daniel Stern[10], and William W. Zhang[11]
[1] Columbia Astrophysics Laboratory, Columbia University, New York, NY 10027, USA; kaya@astro.columbia.edu
[2] Department of Physics, McGill University, Montreal, QC H3A2T8, Canada
[3] Université de Toulouse, UPS-OMP, IRAP, Toulouse, France
[4] CNRS, Institut de Recherche en Astrophysique et Planétologie, 9 Av. colonel Roche, BP 44346, F-31028 Toulouse cedex 4, France
[5] Space Sciences Laboratory, University of California, Berkeley, CA 94720, USA
[6] DTU Space—National Space Institute, Technical University of Denmark, Elektrovej 327, DK-2800 Lyngby, Denmark
[7] Cahill Center for Astronomy and Astrophysics, California Institute of Technology, Pasadena, CA 91125, USA
[8] NASA Marshall Space Flight Center, Huntsville, AL 35812, USA
[9] Lawrence Livermore National Laboratory, Livermore, CA 94550, USA
[10] Jet Propulsion Laboratory, California Institute of Technology, Pasadena, CA 91109, USA
[11] NASA Goddard Space Flight Center, Greenbelt, MD 20771, USA
Received 2014 April 21; accepted 2014 July 24; published 2014 September 10

ABSTRACT

We report on the first hard X-ray detection of the Geminga pulsar above 10 keV using a 150 ks observation with the *Nuclear Spectroscopic Telescope Array* (*NuSTAR*) observatory. The double-peaked pulse profile of non-thermal emission seen in the soft X-ray band persists at higher energies. Broadband phase-integrated spectra over the 0.2–20 keV band with *NuSTAR* and archival *XMM-Newton* data do not fit to a conventional two-component model of a blackbody plus power law, but instead exhibit spectral hardening above ∼5 keV. We find that two spectral models fit the data well: (1) a blackbody ($kT_1 \sim 42$ eV) with a broken power law ($\Gamma_1 \sim 2.0$, $\Gamma_2 \sim 1.4$ and $E_{\rm break} \sim 3.4$ keV) and (2) two blackbody components ($kT_1 \sim 44$ eV and $kT_2 \sim 195$ eV) with a power-law component ($\Gamma \sim 1.7$). In both cases, the extrapolation of the Rayleigh–Jeans tail of the thermal component is consistent with the UV data, while the non-thermal component overpredicts the near-infrared data, requiring a spectral flattening at $E \sim 0.05$–0.5 keV. While strong phase variation of the power-law index is present below ∼5 keV, our phase-resolved spectroscopy with *NuSTAR* indicates that another hard non-thermal component with $\Gamma \sim 1.3$ emerges above ∼5 keV. The spectral hardening in non-thermal X-ray emission as well as spectral flattening between the optical and X-ray bands argue against the conjecture that a single power law may account for multi-wavelength non-thermal spectra of middle-aged pulsars.

Key word: X-rays: individual (Geminga)

Online-only material: color figures

1. INTRODUCTION

Geminga was discovered as a bright GeV source by the *SAS-2* experiment (Thompson et al. 1977). Later, the *ROSAT* X-ray observatory identified it as a pulsar with a 237 ms spin period and a soft thermal spectrum with a blackbody temperature $kT \sim 40$ eV (Halpern & Holt 1992; Bignami & Caraveo 1992). The Energetic Gamma-Ray Experiment Telescope (EGRET) confirmed the pulsations (Bertsch et al. 1992) and measured the pulsar spin-down, establishing that Geminga is a rotation-powered pulsar with a spin-down age $\tau_c \equiv P/2\dot{P} = 3.4 \times 10^5$ yr, a spin-down power $\dot{E} = 3 \times 10^{34}$ erg s^{-1}, and a dipole magnetic field strength $B = 1.6 \times 10^{12}$ G.

Over the last two decades, Geminga has been observed and studied in multi-wavelength bands from radio to TeV (see Bignami & Caraveo 1996 for a review). The Geminga pulsar stands out among thousands of pulsars because it is the second brightest gamma-ray source in our Galaxy with nearly 90% gamma-ray radiation efficiency ($L_\gamma/\dot{E}$) (Caraveo 2014). Its gamma-ray spectrum is well described by a power law with photon index $\Gamma = 1.3$ and an exponential cutoff at $E_c = 2.5$ GeV (Abdo et al. 2010). The gamma-ray emission has been mostly attributed to curvature radiation from relativistic electrons or inverse Compton scattering in the outer gap formed near the light cylinder (Cheng et al. 1986; Romani 1996; Harding et al. 2008; Lyutikov 2013).

After the discovery of pulsations by *ROSAT*, *ASCA* revealed a hard non-thermal component with a power-law index $\Gamma \sim 1.5$ extending to 10 keV (Halpern & Wang 1997). X-ray spectra of middle-aged rotation-powered pulsars are often composed of thermal and non-thermal emission (e.g., Geminga, PSR B0656+14, and PSR B1055−52; De Luca et al. 2005). The bulk of thermal emission from the neutron star (NS) surface is likely due to heat transfer from the NS interior, while non-thermal emission comes from synchrotron radiation in the magnetosphere. A phase-resolved spectroscopic study using deep *XMM-Newton* observations argued for the presence of a second thermal component with a blackbody temperature of $kT \sim 190$ eV (Caraveo et al. 2004) associated with polar caps heated by returning current from the magnetosphere or due to anisotropic heat conduction in the NS crust (Greenstein & Hartke 1983). However, Jackson & Halpern (2005) disputed this claim because phase variation of the non-thermal component can account for the phase-resolved spectra without requiring a second blackbody component. In either case, a second thermal component of the Geminga pulsar, if it exists, is nearly two

orders of magnitude fainter than those of two other middle-aged pulsars, PSR B0656+14 and PSR B1055−52 (De Luca et al. 2005).

Geminga has also been detected at near-infrared (NIR) to UV wavelengths (Bignami et al. 1993; Caraveo et al. 1996; Shibanov et al. 2006; Danilenko et al. 2011), exhibiting two components—a power-law spectrum with $\Gamma \sim 1.4$ and the Rayleigh–Jeans (RJ) tail of the thermal emission detected in the X-ray band (Kargaltsev et al. 2005). Pavlov et al. (1996) demonstrated that joint UV and X-ray spectroscopy is a powerful diagnostic tool to constrain the NS atmospheric composition.

Despite a long-term multi-wavelength observation campaign, the hard X-ray emission (10–100 keV) from Geminga remained undetected due to the lack of sensitive hard X-ray telescopes. In this paper we report on hard X-ray observations of the Geminga pulsar by the *Nuclear Spectroscopic Telescope Array* (*NuSTAR*; Harrison et al. 2013). *NuSTAR* provides the most sensitive probe to date of the Geminga pulsar above 10 keV, with negligible contamination from its faint pulsar wind nebula (PWN) discovered by *Chandra* and *XMM-Newton* (Caraveo et al. 2003; Pavlov et al. 2006, 2010; de Luca et al. 2006). With broadband spectroscopy from *NuSTAR*, archival *XMM-Newton* data, and the published results in NIR to UV bands, we report on new constraints on both the thermal and the non-thermal emission. We use the parallax distance of 250^{+120}_{-62} pc (Faherty et al. 2007), updated from Caraveo et al. (1996), to rule out several thermal models and calculate X-ray luminosities.

The paper is organized as follows. Sections 2 and 3 present the set of observations used and describes our data reduction for *NuSTAR* and *XMM-Newton*, respectively. In this paper, we analyzed 15 *NuSTAR* observations and 9 archival *XMM-Newton* observations (Table 1). Section 4 presents phase-integrated spectroscopy using *NuSTAR* and *XMM-Newton* data jointly. Section 5 presents the *NuSTAR* detection of the pulsations above 10 keV. We compare *NuSTAR* pulse profiles with those from *XMM-Newton* and *Fermi* and study phase variation of the thermal and non-thermal components. Section 6 summarizes our results and discusses their implications for the thermal and non-thermal emission mechanisms of the Geminga pulsar and rotation powered pulsars in general. In Appendices A and B, we show that the absolute *NuSTAR* timestamp is accurate to better than 3 ms, and present a new ephemeris of Geminga based on *XMM-Newton* and *Fermi* data.

2. *NuSTAR* OBSERVATIONS

The *NuSTAR* telescope consists of two co-aligned telescopes with corresponding focal plane modules A and B (FPMA and FPMB). These modules have an angular resolution of 18″ FWHM and 58″ half-power diameter, and an energy resolution of 400 eV (FWHM) at 10 keV (Harrison et al. 2013). The nominal energy band of *NuSTAR* is 3–79 keV. The relative timing accuracy of the *NuSTAR* timestamps is ∼2 ms after correcting for thermal drift of the spacecraft clock. In Appendix B we show that the absolute Barycentric Dynamical Time (TDB) timestamp is accurate to better than ∼3 ms.

A *NuSTAR* observing campaign of the Geminga pulsar was carried out on 2012 September 20–28 in a series of 15 short pointings; an observation log is presented in Table 1. Data products and response files were generated using NuSTARDAS v.1.2.0. The filtered event files produce a total of 148 ks of good exposure time, varying from 2.4 ks to 26.5 ks between pointings. In this work, we limit our analysis from 3 to 20 keV due to low signal-to-noise of the Geminga data at higher energies. Since the source is not variable between the short pointings, we analyzed images and spectra from the combined data set. We used the HEASARC software version 6.13 to analyze both *NuSTAR* and *XMM-Newton* data sets.

Table 1
Observation log of Geminga Pulsar

Obs. ID	Start Date	Instrument	Net Exposure (ks)
		NuSTAR	
30001029002	2012 Sep 20	FPMA/FPMB	7.26
30001029004	2012 Sep 20	FPMA/FPMB	8.81
30001029006	2012 Sep 20	FPMA/FPMB	9.43
30001029008	2012 Sep 21	FPMA/FPMB	4.82
30001029010	2012 Sep 21	FPMA/FPMB	4.95
30001029012	2012 Sep 21	FPMA/FPMB	13.8
30001029014	2012 Sep 25	FPMA/FPMB	2.43
30001029016	2012 Sep 25	FPMA/FPMB	4.36
30001029018	2012 Sep 25	FPMA/FPMB	26.5
30001029020	2012 Sep 26	FPMA/FPMB	6.52
30001029022	2012 Sep 26	FPMA/FPMB	20.9
30001029024	2012 Sep 27	FPMA/FPMB	5.18
30001029026	2012 Sep 27	FPMA/FPMB	4.33
30001029028	2012 Sep 27	FPMA/FPMB	23.3
30001029030	2012 Sep 28	FPMA/FPMB	5.00
		XMM-Newton[a]	
0111170101	2002 Apr 4	PN/MOS1/MOS2	58.5/80.4/80.1
0201350101	2004 Mar 13	PN/MOS1/MOS2	12.3/16.5/17.1
0301230101	2005 Sep 16	PN[b]	6.59
0311591001	2006 Mar 17	PN/MOS1/MOS2	19.0/25.2/23.8
0400260201	2006 Oct 2	PN/MOS1/MOS2	13.7/18.9/18.9
0400260301	2007 Mar 11	PN/MOS1/MOS2	15.0/20.5/20.0
0501270301	2008 Mar 8	PN/MOS1/MOS2	7.98/10.9/10.6
0550410201	2008 Oct 3	PN/MOS1/MOS2	14.0/18.6/17.6
0550410301	2009 Mar 10	PN/MOS1/MOS2	7.40/10.0/9.23

Notes.
[a] In all *XMM-Newton* observations, the PN camera was operated in Small Window mode with the thin filter, and both MOS cameras were operated in Full Frame mode with the medium filters. We did not use *XMM-Newton* data from observation 0501270201 in 2007 September due to an attitude reconstruction issue.
[b] MOS cameras were not operating in this observation.

2.1. Imaging Analysis

First, we constructed mosaic maps by combining data from all the observations following Nynka et al. (2013). We registered the known *Hubble Space Telescope* (*HST*) position of the Geminga pulsar (Faherty et al. 2007). We generated exposure maps using `nuexpomap` and merged the exposure-corrected images. Figure 1 shows the mosaic image of the Geminga pulsar in the 3–10 and 10–20 keV energy bands. Given *NuSTAR*'s angular resolution, the bright source in Figure 1 is consistent with being a point source. The pulsar was not visible above 20 keV, the point at which the instrument background exceeds the source strength.

We searched for serendipitous point sources in the *NuSTAR* mosaic images using `wavdetect`. In the 3–10 keV band, we detected a known narrow-line active galactic nucleus at $z = 0.891$ (NuSTAR J063358+1742.4) $\sim 4'$ south of the Geminga pulsar (Alexander et al. 2013). None of the faint PWN features around the pulsar (Pavlov et al. 2010) are visible because they are swamped by the brighter pulsar emission and *NuSTAR* background photons.

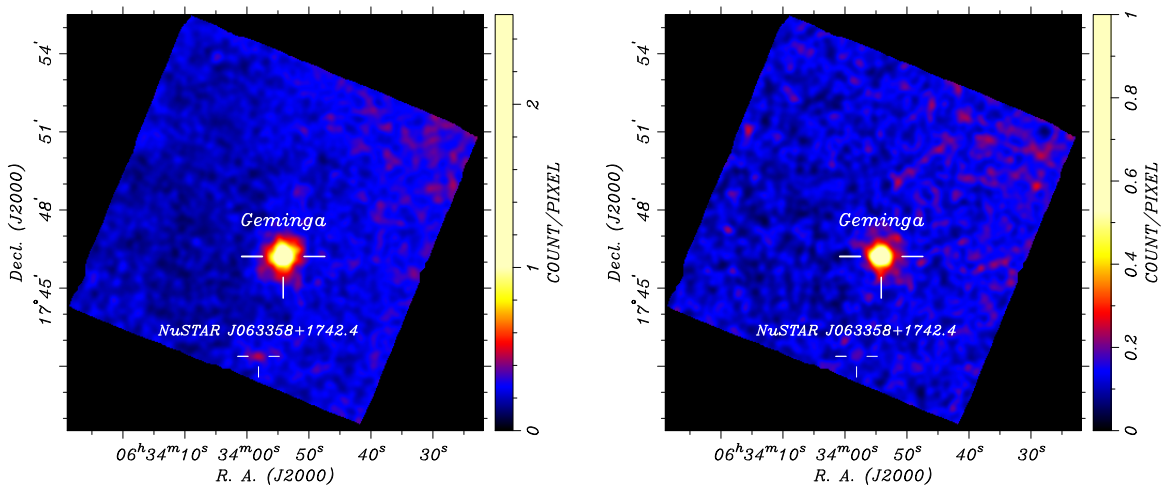

Figure 1. *NuSTAR* mosaic image of the field containing the Geminga pulsar, in the 3–10 keV (left) and 10–20 keV (right) bands. Data from all Geminga *NuSTAR* observations and modules are merged, with appropriate exposure corrections applied. The locations of Geminga and NuSTAR J063358+1742.4, as determined using wavedetect, are indicated by the tick marks.

(A color version of this figure is available in the online journal.)

2.2. Spectral Extraction and Nebular Contamination

For spectral analysis, we extracted source spectra from a circular aperture with 30″ radius centered at the Geminga pulsar position and background spectra using a $60'' < r < 120''$ annulus. Since each detector chip has a different internal background level, it is important to extract background spectra from the same detector chip where the source was located (detector 0 in all observations of Geminga). To assess the robustness of our results with respect to the choice of background region, we also extracted background spectra from several circular regions with radius 90″ on detector chip 0, finding the results only changed by a small fraction of the statistical uncertainty. For the subsequent spectral analysis, we limit the energy band to below 20 keV, above which the background becomes dominant with several strong emission lines at ∼20–30 keV.

To assess contamination from the PWN, we estimated *NuSTAR* count rates using Table 1 in Pavlov et al. (2010) for the brightest PWN feature, the "A-tail." We predict 5×10^{-4} (3–10 keV) and 3×10^{-4} counts s^{-1} (10–30 keV) within an $r = 30''$ (equal to the half-power radius) circle. These estimated count rates are ∼5–7 times smaller than the combined count rate of the *NuSTAR* background and pulsar at the location of the PWN. Furthermore, using archival *Chandra* data from 2012 and 2013, we found that the overall contamination from the PWN features within 30″ of the pulsar is less than 5% and is thus below our statistical uncertainties (see Pavlov et al. 2006, 2010 and de Luca et al. 2006 for the individual PWN features and their positions/fluxes).

3. *XMM-Newton* OBSERVATIONS

We analyzed nine archival *XMM-Newton* observations of the Geminga pulsar from 2002 to 2009 (see Table 1), reduced using the Standard Analysis Software *SAS v.12* and the most up-to-date calibration files. The EPIC-PN data, acquired in high time-resolution `SmallWindow` mode (6 ms readout), are most suitable for our timing and spectral analysis; the 0.3 s EPIC-MOS data suffer from photon pile-up and are not used here. The data reduction and analysis follow the studies of Caraveo et al. (2004), Jackson & Halpern (2005), and De Luca et al. (2005). After filtering out background flares using the EPIC-PN count rate threshold of 0.05 counts s^{-1} above 10 keV, we obtained a total exposure time of 154.5 ks.

For spectral analysis, we extracted source counts from a circular aperture with a radius of 15″ centered on the source position, computed using the *SAS* `emldetect` routine. We chose a small source extraction compared to previous studies to optimize the high-energy (>4 keV) signal-to-noise ratio at the expense of the low energy throughput. Background spectra are extracted from a region with a radius of 30″ placed at the same CCD column for each observation, to avoid the faint PWN features (Pavlov et al. 2006). We combined all *XMM-Newton* EPIC-PN spectra using the `FTOOL` `addascaspec` and performed spectral fitting in the 0.25–10 keV band.

4. JOINT SPECTRAL ANALYSIS WITH *NuSTAR* AND *XMM-Newton*

We analyzed *NuSTAR* and *XMM-Newton* spectra of the Geminga pulsar by jointly fitting multiple spectra using XSPEC 12.8. We grouped each spectrum by a minimum of 30 counts per bin. When we fit multiple data jointly, we used a multiplicative factor (`const` command in XSPEC) for each data set in order to take into account the small flux calibration errors (<10%) between *XMM-Newton* and *NuSTAR*. We adopted 1σ (68% c.l.) errors for all the spectral fitting results presented in this paper. In order to distinguish between different spectral models, we used χ^2 statistics and the *F*-test (`ftest` command in XSPEC) as a null hypothesis test.

4.1. Non-thermal Spectral Fitting Above 3 keV

Thermal and non-thermal components in pulsar X-ray spectra can be strongly covariant with inherent parameter degeneracy. In order to constrain the non-thermal component cleanly, we analyzed the X-ray spectra above 3 keV where the contribution from the second blackbody component is negligible (De Luca et al. 2005). We note that the low absorption column ($\sim 10^{20}$ cm^{-2}) does not affect the Geminga spectra above 3 keV. The 3–20 keV *NuSTAR* spectra are well fit to a single power-law model with $\Gamma = 1.35 \pm 0.08$ and a reduced χ^2 of 0.97 (49 degrees of freedom, dof). In order to improve the photon statistics, we jointly fit 3–20 keV *NuSTAR* spectra and 3–10 keV

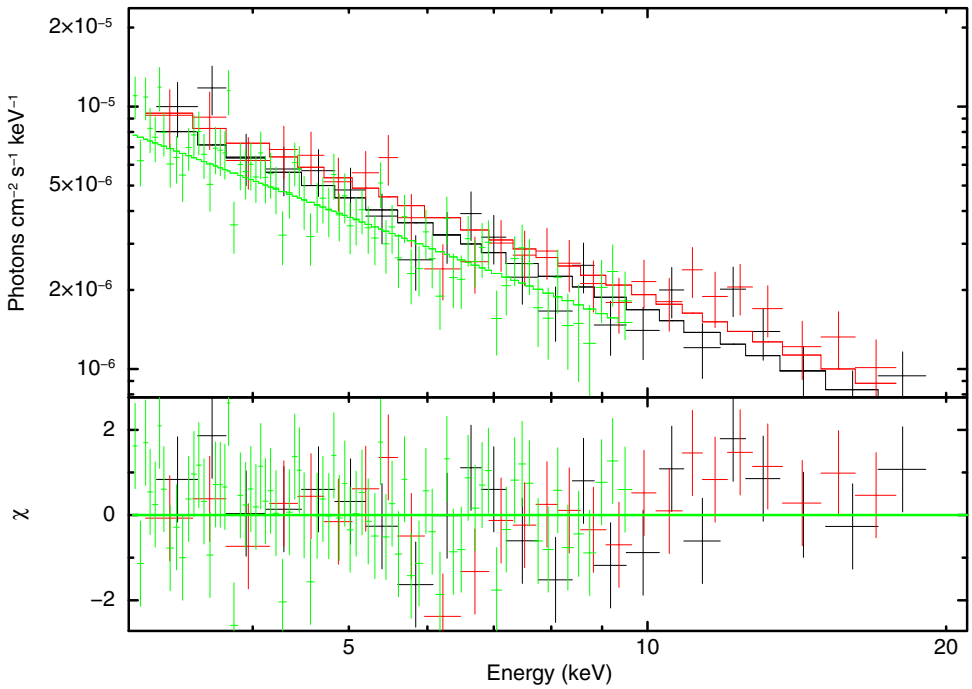

Figure 2. Unfolded 3–20 keV *NuSTAR* + *XMM-Newton* EPIC-PN spectra of the Geminga pulsar fit with a single power-law model. The green, black, and red data points are for *XMM-Newton* EPIC-PN, *NuSTAR* FPMA, and FPMB, respectively.

(A color version of this figure is available in the online journal.)

Table 2
Joint Phase-averaged Spectral Fitting with *NuSTAR* and *XMM-Newton* Data

Parameters	PL ($E > 3$ keV)	BB+PL	2BB+PL	BB+2PL	BB+BKPL
$N_{\rm H}$ (10^{20} cm^{-2})	...	1.31 ± 0.21	1.54 ± 0.26	2.16 ± 0.28	1.93 ± 0.24
kT_1 (eV)[a]	...	44.4 ± 0.6	44.0 ± 0.8	41.6 ± 0.8	42.4 ± 0.6
R_1 (km)[b]	...	10.7 ± 0.8	11.4 ± 1.1	15.1 ± 1.6	13.7 ± 1.2
kT_2 (eV)[a]	...	...	195 ± 14	...	...
R_2 (m)[b]	...	...	45 ± 7	...	...
Γ_1	1.44 ± 0.06	1.90 ± 0.02	1.70 ± 0.04	2.15 ± 0.08	2.04 ± 0.03
$N_{\rm PL1}$[c]	7.7 ± 0.1	6.0 ± 0.3	7.8 ± 0.3	8.0 ± 0.1	3.7 ± 0.4
Γ_2	...	...	...	0.37 ± 0.44	1.42 ± 0.07
$N_{\rm PL2}$, $E_{\rm break}$[d]	...	...	...	0.24 ± 0.24	3.4 ± 0.3
χ^2/dof	0.968	1.063	0.991	0.889	0.904
dof	121	449	447	446	446

Notes.

[a] kT_1 and kT_2 are the best-fit temperatures for the first and second blackbody components, respectively.

[b] R_1 and R_2 are the best-fit radii for the first and second blackbody components, respectively. A distance of 250 pc from Faherty et al. (2007) is assumed. The uncertainty on the measured distance (250^{+120}_{-62} pc) is not taken into account.

[c] The units of 10^{-5} photons cm^{-2} s^{-1} keV^{-1} at $E = 1$ keV.

[d] Break energy ($E_{\rm break}$ (keV)) for BB+BKPL model. Power-law flux normalization ($N_{\rm PL2}$ (10^{-5} photons cm^{-2} s^{-1} keV^{-1}) at $E = 1$ keV) for the other models.

XMM-Newton EPIC-PN spectra. Figure 2 shows the spectral fits and residuals, yielding $\Gamma = 1.44 \pm 0.06$ and a reduced χ^2 of 0.97 (121 dof). We find that a single power-law fit is adequate; any additional continuum component such as a blackbody or a second power-law model did not improve the spectral fit significantly, with F-test false probabilities of ~0.02. The power-law index from the 3–20 keV spectra is consistent with that of Kargaltsev et al. (2005) ($\Gamma = 1.56 \pm 0.24$) where they fit *XMM-Newton* EPIC-PN spectra in 2.5–10 keV, but our broadband data provide stricter constraints.

4.2. Broadband Spectral Fitting Between 0.2 and 20 keV

We analyzed broadband X-ray spectra of the Geminga pulsar in the 0.25–20 keV band with 3–20 keV *NuSTAR* spectra and 0.25–10 keV *XMM-Newton* EPIC-PN spectra. We use the `tbabs` absorption model in XSPEC, with Wilms abundances and Verner cross-sections (Wilms et al. 2000; Verner et al. 1996). First, we fit a blackbody plus power-law (BB+PL) model to the *NuSTAR* plus *XMM-Newton* EPIC-PN spectra. The fit parameters are consistent with the previous analysis of Jackson & Halpern (2005) (Table 2). However, some residual excesses are clearly seen above ~5 keV, indicating the presence of an additional spectral component (Figure 3). The fit power-law index ($\Gamma = 1.90 \pm 0.02$) is softer than that from the 3–20 keV spectral analysis ($\Gamma = 1.44 \pm 0.06$). A similar discrepancy in the fit power-law index between the entire band and high-energy band was previously reported by Kargaltsev et al. (2005) using only *XMM-Newton* EPIC-PN data.

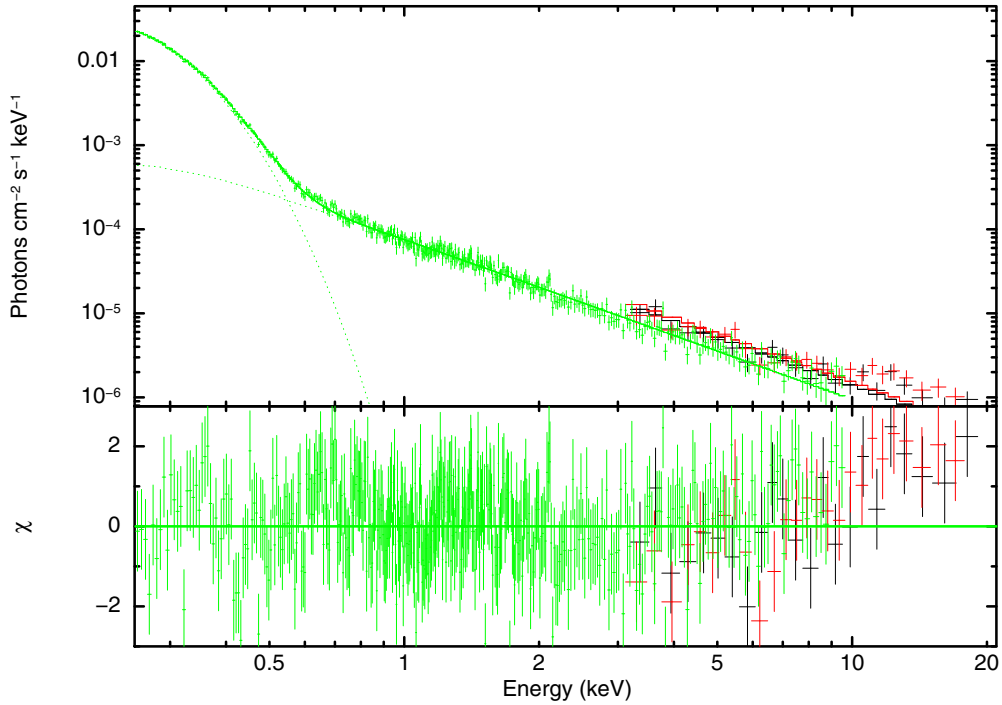

Figure 3. Unfolded 0.25–20 keV *NuSTAR* and *XMM-Newton* (EPIC-PN) spectra of the Geminga pulsar fitted with the BB+PL model. Residuals are seen especially in the *NuSTAR* data above 10 keV.

(A color version of this figure is available in the online journal.)

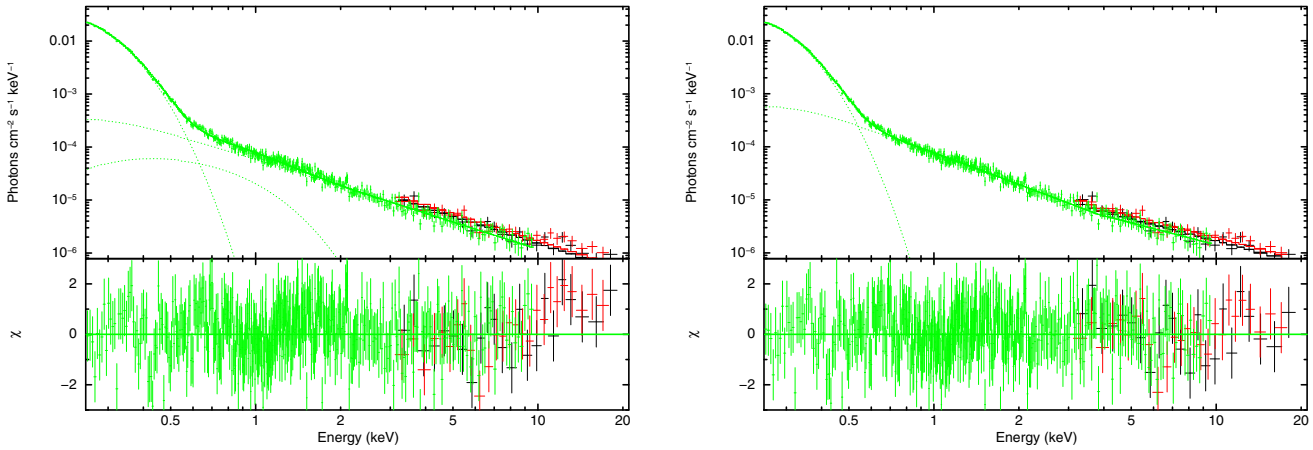

Figure 4. Unfolded 0.25–20 keV *NuSTAR* and *XMM-Newton* (EPIC-PN) spectra of the Geminga pulsar fitted with 2BB+PL (left) and BB+BKPL model (right).

(A color version of this figure is available in the online journal.)

Instead of a blackbody model, we also fit a magnetized hydrogen NS atmosphere model for the surface magnetic field $B = 10^{12}$ G (nsa in XSPEC; Pavlov et al. 1995). For a given effective temperature, a NS hydrogen atmosphere spectrum is harder than a blackbody because the dominant free–free absorption opacity decreases with photon energy. Although the fit quality and residuals are similar to those of the blackbody model fit, the NS hydrogen atmosphere model yields a radius ($R = 440 \pm 60$ km) that is inconsistent with any proposed models for the NS equation of state (Lattimer & Prakash 2007). In addition, the RJ tail in the UV band is significantly overestimated because the thermal flux in the RJ tail is proportional to $R^2 \times T$ (Kargaltsev et al. 2005). Therefore we rule out the NS hydrogen atmosphere model, and hereafter we use only a blackbody as a thermal model.

Given the excess residuals from fitting the BB+PL model, we fit three different models either adding a blackbody or power-law model or using a broken power law as the non-thermal component. Specifically, we fit two blackbodies plus a power law (2BB+PL), a blackbody plus two power laws (BB+2PL) and a blackbody plus broken power law (BB+BKPL, with `bknpower` model in XSPEC). All three models greatly improved the spectral fit compared to the BB+PL model with F-test false probabilities $<10^{-7}$. Figure 4 shows the *NuSTAR* and *XMM-Newton* spectra fit by the 2BB+PL and BB+BKPL models. All three models (BB+BKPL, BB+2PL, and 2BB+PL) agree reasonably well with the UV data (i.e., the RJ tail of the X-ray thermal emission). However, we find the BB+2PL model unphysical and exclude it in the following sections since its second power-law component with $\Gamma \sim 0.4$ exceeds the spin-down power of Geminga.

We find any additional continuum component is either not statistically required or does not yield reasonable results. For example, although an additional (third) blackbody component

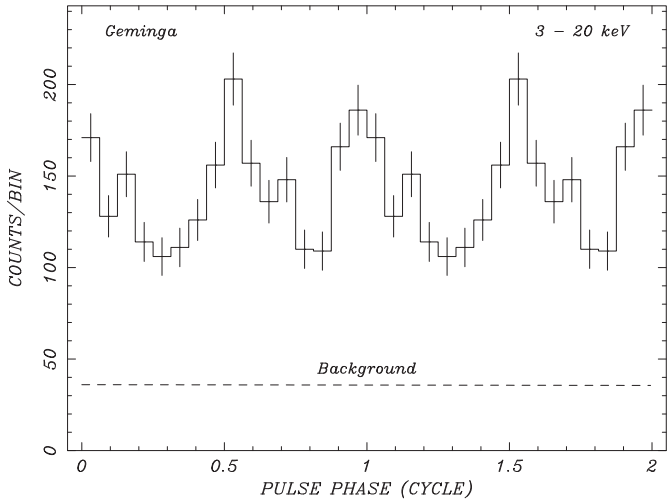

Figure 5. *NuSTAR* pulse profile of the Geminga pulsar in the 3–20 keV band. Photon arrival times were folded on the ephemeris given in Table 3. Two cycles are displayed for clarity.

to the 2BB+PL model further improves the fit, the model (3BB+PL) overpredicts the UV data by a factor of ∼3 and the fit radius is too large for reasonable NS models ($R = 27 \pm 7$ km). Therefore we rule out the 3BB+PL model.

Kargaltsev et al. (2005) pointed out that the *XMM-Newton* spectrum hardens around $E \sim 5$ keV. With the inclusion of *NuSTAR* data up to 20 keV we find that this hardening is even more pronounced. The hard power-law index of ∼1.5 above 3 keV reported in Section 4.1 supports this result.

5. PULSE PROFILE AND PHASE-RESOLVED SPECTRAL ANALYSIS

In this section, we present *NuSTAR* pulse profiles and phase-resolved spectral analysis. Using *NuSTAR* data of the pulsar B1509−58 as well as long-term *XMM-Newton* and *Fermi* data of Geminga, we were able to determine the *NuSTAR*'s absolute timing accuracy to better than 3 ms and derive a new ephemeris solution of Geminga (see Appendices A and B for details). We extracted source photons from an 44″ radius aperture and 3–20 keV energy band, optimal for detecting pulsations. Figure 5 presents the *NuSTAR* pulse profile of Geminga folded on the *Fermi* ephemeris (Table 3 in Appendix A). The intrinsic pulsed fraction in the 3–20 keV *NuSTAR* detection band is $f_p \approx 43\%$ (Figure 5). The broadband profile contains 1850 background subtracted counts collected during 154 ks of lifetime that spanned the 8 day data set. The signal strength of $Z_3^2 = 82.3$ has a negligible false detection probability ($\wp = 1.2 \times 10^{-13}$).

For comparison, Figure 6 presents *XMM-Newton* pulse profiles in four energy bands, along with the *NuSTAR* (10–20 keV) and *Fermi* (0.3–10 GeV) pulse profiles, all folded on the *Fermi* ephemeris given in Table 3. We verified that the two broad peaks in the *NuSTAR* pulse profile are statistically identical to the *XMM-Newton* profile in the overlapping 3–10 keV energy band.

Given that the double-peaked pulse profile is persistent over the 3–20 keV band where non-thermal emission is dominant, it is possible that the observed spectral hardening is due to phase variation of the non-thermal component. Indeed, Jackson & Halpern (2005) demonstrated that the photon index of the non-thermal component varies strongly with phase. First, we performed phase-resolved spectroscopy using only the

Table 3
Geminga Ephemeris

Parameter	Value
Epoch of coordinates (MJD)[a]	49794.0
R.A. (J2000)	$06^h33^m54^s.153$
Decl. (J2000)	$+17°46'12''.91$
R.A. proper motion, $\mu_\alpha \cos\delta$	142.2 ± 1.2 mas yr^{-1}
Decl. proper motion, μ_δ	107.4 ± 1.2 mas yr^{-1}
XMM-Newton Timing Solution (2002 Apr 5–2009 Mar 10)	
Epoch of ephemeris (MJD)[b]	53630.0 (TDB)
Span of ephemeris (MJD)	52369–54900
Frequency, f	4.21758680107(16) Hz
Frequency derivative, $\dot{f}$	$-1.952196(17) \times 10^{-13}$ Hz s^{-1}
Frequency second deriv., $\ddot{f}$	$-3.20(90) \times 10^{-25}$ Hz s^{-2}
Period, P	0.2371024112050(90) s
Period derivative, $\dot{P}$	$1.0974768(96) \times 10^{-14}$
Period second deriv., $\ddot{P}$	$1.90(51) \times 10^{-26}$
Fermi Timing Solution (2008 Aug 4–2012 Oct 12)	
Epoch of ephemeris (MJD)[b]	55440.0 (TDB)
Span of ephemeris (MJD)	54682–56212
Frequency, f	4.217556269653(16) Hz
Frequency derivative, $\dot{f}$	$-1.9521993(37) \times 10^{-13}$ Hz s^{-1}
Frequency second deriv., $\ddot{f}$	$5.64(33) \times 10^{-25}$ Hz s^{-2}
Period, P	0.23710412761897(90) s
Period derivative, $\dot{P}$	$1.0974946(21) \times 10^{-14}$
Period second deriv., $\ddot{P}$	$-3.07(19) \times 10^{-26}$

Notes.
[a] Coordinates used to barycenter photon arrival times, based on *HST* measurements (Caraveo et al. 1998) and the proper motion results of Faherty et al. (2007).
[b] Phase zero in Figures 5 and 6.

XMM-Newton EPIC-PN data. We extracted *XMM-Newton* EPIC-PN spectra from 10 phase intervals of $\Delta\phi = 0.1$ width using the ephemeris in Table 3 (see Figure 6 for the folded light curves). We followed the phase-integrated spectral analysis regarding background subtraction, spectral binning, and statistical tests. Following Jackson & Halpern (2005), we fit a BB+PL model to each of the phase-resolved spectra in the 0.25–10 keV band with the absorption column $N_{\rm H}$ fixed to the value from the phase-integrated spectral analysis ($N_{\rm H} = 1.3 \times 10^{20}$ cm^{-2}; see Table 2). Spectral fitting with the BB+PL model was adequate for all phase-resolved spectra.

We then let kT, Γ, and the flux normalizations vary freely. The blackbody temperature remains nearly constant around $kT = 44$ eV (left panel in Figure 7). On the other hand, the power-law index strongly varies with phase (Figure 8) from $\Gamma = 1.59 \pm 0.06$ at $\phi = 0.2$–0.3 to $\Gamma = 2.14 \pm 0.06$ at $\phi = 0.8$–0.9, confirming the results of Jackson & Halpern (2005). It is noteworthy that the non-thermal spectrum is hardest when the flux normalization is at its minimum ($\phi = 0.2$–0.3).

We also studied the phase variation of the *NuSTAR* spectra. Given the limited statistics of the *NuSTAR* data, we extracted two phase-resolved *NuSTAR* spectra from $\phi = 0.0$–0.3 and 0.9–1.0 (phase A) and $\phi = 0.3$–0.9 (phase B). Phase A and B represent the phase intervals where the *XMM-Newton* power-law indices are harder ($\Gamma = 1.5$–1.8) and softer ($\Gamma = 1.9$–2.2), respectively. Since the non-thermal component completely dominates above 3 keV (even for the 2BB+PL model), we fit a single PL model to the *NuSTAR* spectra in three different energy bands. In the 3–20 keV band, both the phase A and B *NuSTAR* spectra fit to $\Gamma = 1.4 \pm 0.1$. In the 3–10 keV band, phase A and B *NuSTAR*

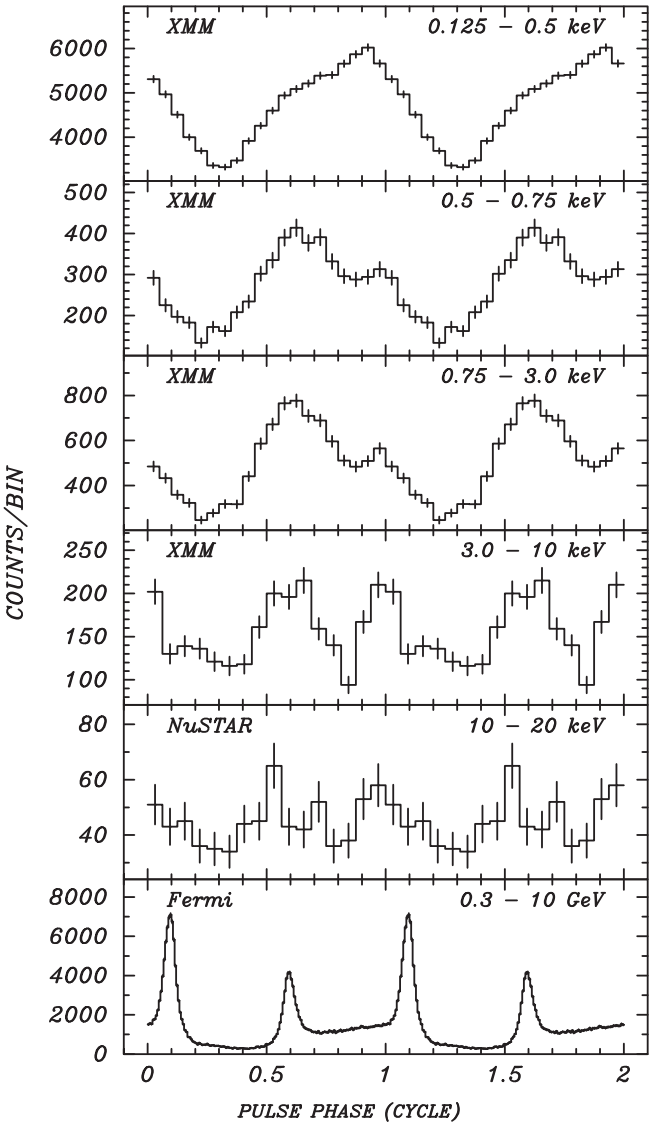

Figure 6. Pulse profiles of the Geminga pulsar from several missions and epochs, *XMM-Newton*: 0.125–0.5 keV, 0.5–0.75 keV, 0.75–3.0 keV, 3.0–10.0 keV, *NuSTAR*: 10–20 keV, and *Fermi*: 0.3–10 GeV, from top to bottom, respectively. Photon arrival times for *NuSTAR* and *Fermi* data sets are folded on the *Fermi* ephemeris given in Table 3. The *Fermi* profile includes data that span from the end of the *XMM-Newton* epoch (2008 August 4) to the *NuSTAR* (2012 October 11) observations. Photon arrival times for *XMM-Newton* data sets are folded on the *XMM-Newton* ephemeris of Table 3. Two cycles are displayed for clarity.

spectra yield $\Gamma = 1.4 \pm 0.2$ and 1.8 ± 0.2, similar to the phase variation found in the *XMM-Newton* data. On the other hand, in the 5–20 keV band, phase A and B *NuSTAR* spectra exhibited harder power-law indices with $\Gamma = 1.4 \pm 0.2$ and 1.2 ± 0.2, respectively. This suggests that there is another non-thermal component emerging above 5 keV where we observed spectral hardening in the phase-integrated spectral analysis.

6. DISCUSSION

6.1. Thermal Emission

Conventionally, X-ray spectra of middle-aged pulsars have been interpreted as a combination of thermal and non-thermal emission. Thermal emission is thought to have two components—a cold temperature component from the NS surface and a hot temperature component from the heated polar caps. Two middle-aged pulsars, PSR B0656+14 and PSR B1055−52, exhibit two thermal components and a non-thermal component (De Luca et al. 2005). It has also been a common exercise to fit the X-ray spectra of the Geminga pulsar to either one or two blackbody components (Halpern & Ruderman 1993; Halpern & Wang 1997; Jackson et al. 2002; Caraveo et al. 2004; De Luca et al. 2005; Jackson & Halpern 2005; Kargaltsev et al. 2005).

Our spectral analysis rules out the hydrogen atmosphere model since it overpredicts the UV flux and the fit radius is too large for NS. Similarly, a model with three blackbody components is ruled out. Our best-fit models have either a single blackbody component (requiring a break in the non-thermal component) or two blackbody components (2BB+PL model). Our spectral analysis showed a second blackbody component is not present, or is faint, with a bolometric luminosity of $L_x \sim 9 \times 10^{29}$ erg s^{-1}—this is smaller than those of PSR B0656+14 and PSR B1055−52 by more than an order of magnitude.

Based on previous theoretical work, hot polar caps can be faint either because they may not be fully visible to an observer or they are not sufficiently heated to emit observable thermal X-rays. Cheng & Zhang (1999) studied various thermal components including hot polar caps heated by returning current from the outer gaps and found that the visibility of these thermal components and their relative strengths compared to non-thermal emission strongly depends on the viewing angle between the dipole magnetic axis and the observer's line of sight and the inclination angle between the rotational and the

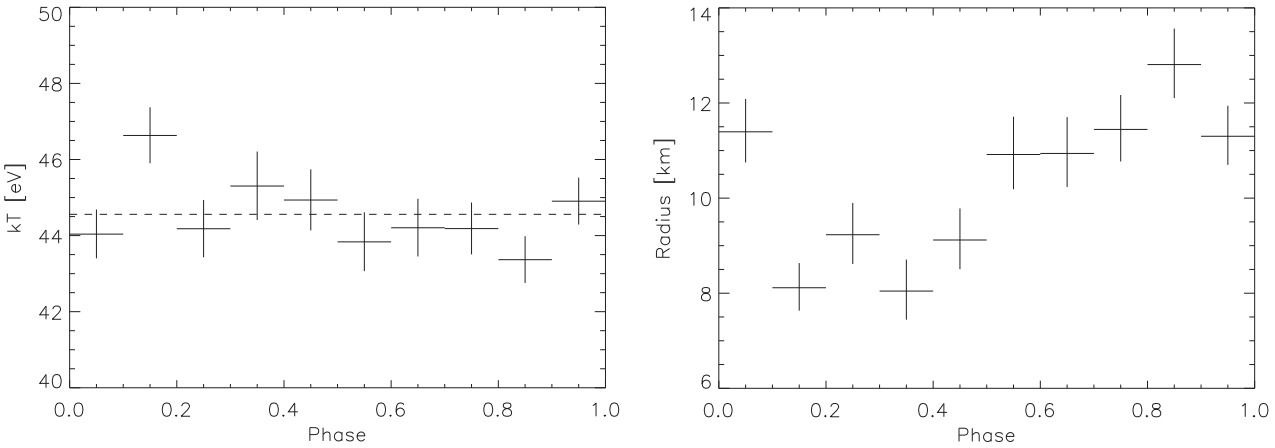

Figure 7. Phase variation of the fitted blackbody temperature (left) and radius at $d = 250$ pc (right). *XMM-Newton* data in the 0.25–10 keV band were used for spectral fitting. The phase zero is identical to that of the folded light curves in Figure 6.

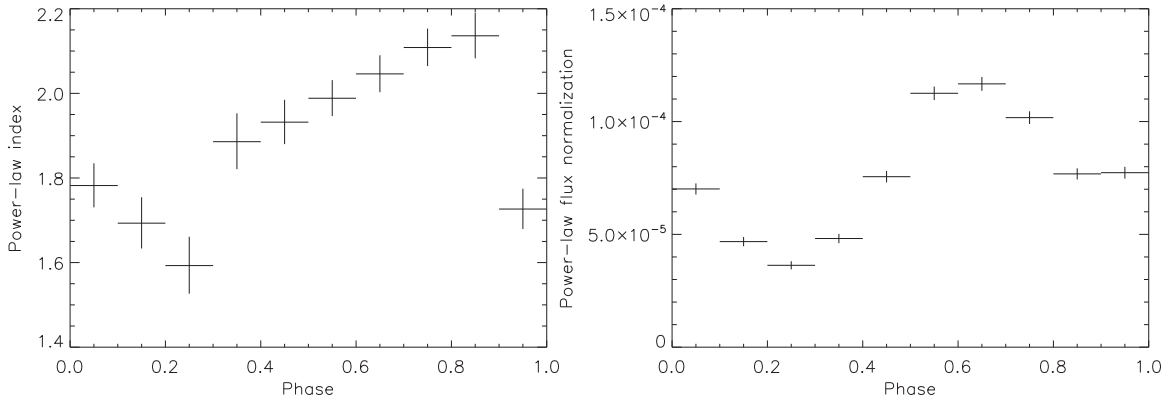

Figure 8. Phase variation of the best-fit power-law index (left) and flux normalization (photons cm^{-2} s^{-1} keV^{-1}) at $E = 1$ keV (right) in the 0.25–10 keV band. *XMM-Newton* data in the 0.25–10 keV band were used for spectral fitting. The phase zero is identical to that of the folded light curves in Figure 6.

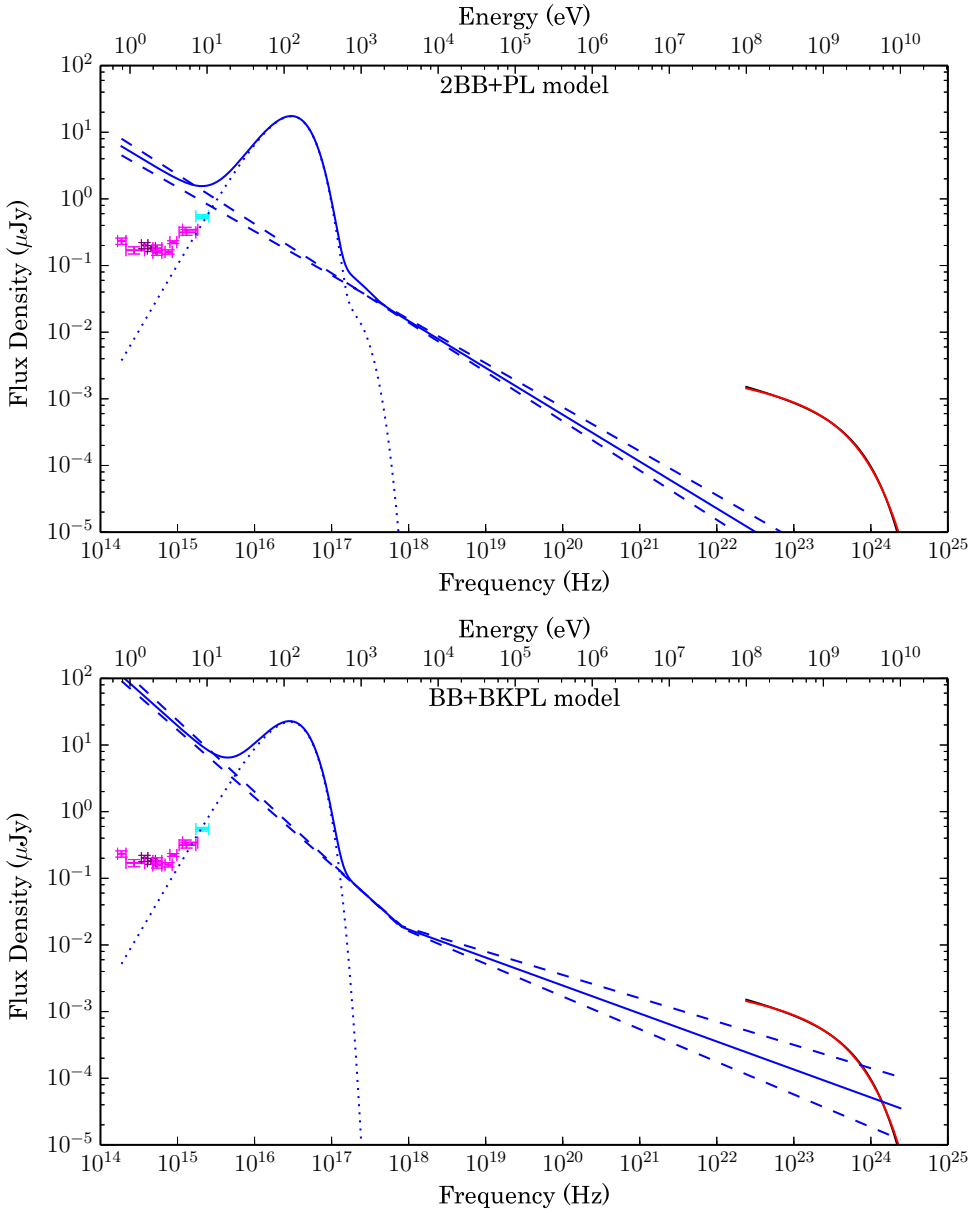

Figure 9. Spectral energy distribution of the Geminga pulsar for two different model fits (top: 2BB+PL, bottom: BB+BKPL). Magenta points are *HST* imaging fluxes, purple points show Subaru imaging fluxes, and the cyan point is from a power-law fit to *HST*/STIS data, all of which have been dereddened (Kargaltsev et al. 2005; Shibanov et al. 2006). The red lines are an exponentially cutoff power-law fit to the *Fermi* phase-integrated spectrum (Abdo et al. 2010). The blue lines are the best-fit models to *NuSTAR* and *XMM-Newton* data between 0.25 and 20 keV. The dotted lines indicate thermal components, while the dashed lines indicate 68% error envelopes of the non-thermal components.

(A color version of this figure is available in the online journal.)

dipole magnetic axes. Indeed, Cheng & Zhang (1999) predicted that hard thermal X-rays from hot polar caps might not be visible because the viewing angle is larger than the inclination angle. This was also independently concluded by Romani & Yadigaroglu (1995) who applied their gamma-ray emission models to the EGRET spectra and light curves of the Geminga pulsar.

Alternatively, Wang et al. (1998) argued that relativistic electrons and positrons traveling from the outer gaps toward polar caps may undergo very efficient cooling by resonant inverse Compton scattering on radio photons, in addition to cooling by curvature radiation. However, in this scenario, it is not clear why Geminga is unique with fainter hot polar cap emission compared to other middle-aged pulsars.

6.2. Non-thermal Spectral Hardening and Broadband Spectral Energy Distribution

Most pulsar emission models attribute non-thermal X-ray emission to electron synchrotron radiation in the magnetosphere. Wang et al. (1998) predicted a power-law spectrum with $\Gamma \sim 1.5$ in the X-ray band. Our spectral analysis suggests a spectral hardening at $E \sim 5$ keV in the non-thermal component. Interestingly, the Vela pulsar, another middle-aged pulsar with a spin-down age of 10^4 yr, exhibits similar spectral hardening in the pulsed spectra obtained by *RXTE* (Harding et al. 2002).

After re-analyzing archival data from *Spitzer Space Telescope*, Danilenko et al. (2011) studied the non-thermal emission of the Geminga and Vela pulsars across the mid-infrared, optical, and X-ray bands. For both pulsars as well as the Crab pulsar, non-thermal spectra in the optical band are significantly flatter than those in the X-ray band (Danilenko et al. 2011). In all our best-fit models, an extension of the non-thermal spectra from the X-ray to lower frequencies overpredicts the optical fluxes (Figure 9). Therefore, it is evident that some spectral flattening takes place somewhere between ∼0.05 and 0.5 keV.

This spectral evolution between the optical and X-ray band is conceivable from a theoretical point of view. Wang et al. (1998) pointed out that the electron cyclotron cutoff energy may be $E_c \sim 0.1$ keV in the magnetosphere where the magnetic field strength ($B \sim 10^{10}$ G) is significantly weaker than on the NS surface ($B_S = 1.6 \times 10^{12}$ G). Below the cyclotron cutoff energy, which was estimated to be ∼0.02–0.5 keV, the spectrum should have the canonical low-energy synchrotron index of $\Gamma \sim 2/3$, much harder than the X-ray synchrotron spectra with $\Gamma \sim 1.5$ (Wang et al. 1998).

Toward higher energies, an extension of the BB+BKPL model ($\Gamma_2 \sim 1.4$) is roughly consistent with the phase-averaged *Fermi* spectrum with $\Gamma \sim 1.3$ (Abdo et al. 2010), while the 2BB+PL is inconsistent with direct extrapolation to the *Fermi* band (see Figure 9). However, most theoretical models predict X-ray synchrotron spectra will become weaker in the MeV range until different emission mechanisms (e.g., curvature radiation and inverse Compton) emerge toward the GeV band (Romani 1996); this is indeed what was observed in the pulsed spectra of the Crab and Vela pulsars. Wang et al. (1998) estimated a high-energy cutoff of X-ray synchrotron spectra at ∼5 MeV. Some models also predict that one could observe synchrotron, inverse Compton, and curvature radiation dominating at different energies, and therefore expect multiple power-law components between the X-ray and GeV bands (Harding et al. 2008). None of these models argues that the slope of the non-thermal X-rays (which is due to synchrotron radiation) and that of the GeV gamma-rays should be the same.

In summary, our spectral analysis confirms the spectral hardening at $E \sim 5$ keV, and indicates that a comparison between the optical and X-ray non-thermal spectra requires a spectral flattening toward low energy between ∼0.05 and 0.5 keV. Thus, the Geminga pulsar should have two spectral breaks in its multi-wavelength non-thermal spectrum, in addition to spectral evolution from the X-ray to GeV bands as predicted by a handful of pulsar emission models. The multiple spectral break scenario argues against the view of Durant et al. (2011) where a single power-law model might account for the multi-wavelength non-thermal spectra of middle-aged pulsars.

7. CONCLUSION

Our 150 ks *NuSTAR* observation of the Geminga pulsar detects pulsed emission above 10 keV for the first time. The power-law spectrum and the double-peaked pulse profile, previously seen in the 3–10 keV soft band, persist above 10 keV. By combining *NuSTAR* and archival *XMM-Newton* data, our broadband spectroscopy from 0.2 to 20 keV is able to constrain both the thermal and non-thermal emission from the pulsar. Our broadband spectral analysis from NIR to the hard X-ray band detects spectral hardening at $E \sim 5$ keV and also indicates spectral flattening between the optical and hard X-ray bands, similar to what is seen in the Vela pulsar. It will be intriguing to observe other middle-aged pulsars with *NuSTAR* to search for spectral breaks in the (hard) X-ray band.

This work was supported under NASA Contract No. NNG08FD60C, and made use of data from the *NuSTAR* mission, a project led by the California Institute of Technology, managed by the Jet Propulsion Laboratory, and funded by the National Aeronautics and Space Administration. We thank the *NuSTAR* Operations, Software, and Calibration teams for support with the execution and analysis of these observations. This research has made use of the *NuSTAR* Data Analysis Software (NuSTARDAS) jointly developed by the ASI Science Data Center (ASDC, Italy) and the California Institute of Technology (USA). E.V.G. acknowledges support from NASA/Fermi grant NNX12AO89G and NASA/Chandra grant G03-14066X. V.M.K. acknowledges support from an NSERC Discovery Grant, the FQRNT Centre de Recherche Astrophysique du Quebec, an R. Howard Webster Foundation Fellowship from the Canadian Institute for Advanced Research (CIFAR), the Canada Research Chairs Program, and the Lorne Trottier Chair in Astrophysics and Cosmology. A.M.B. acknowledges the support by NASA grants NNX10AI72G and NNX13AI34G.

APPENDIX A

TIMING ANALYSIS AND DERIVATION OF A NEW EPHEMERIS OF GEMINGA

To allow a joint phase-resolved spectral analysis of the *XMM-Newton* and the *NuSTAR* Geminga data we require phase-connected timing solutions spanning the two missions. The *XMM-Newton* data itself is suitable for self-generating a phase-connected timing solution as the data were obtained for this purpose. The ephemeris presented here bridges the gap between the end of the EGRET and the start of the *Fermi* mission. As the *XMM-Newton* observations do not overlap with the *NuSTAR*

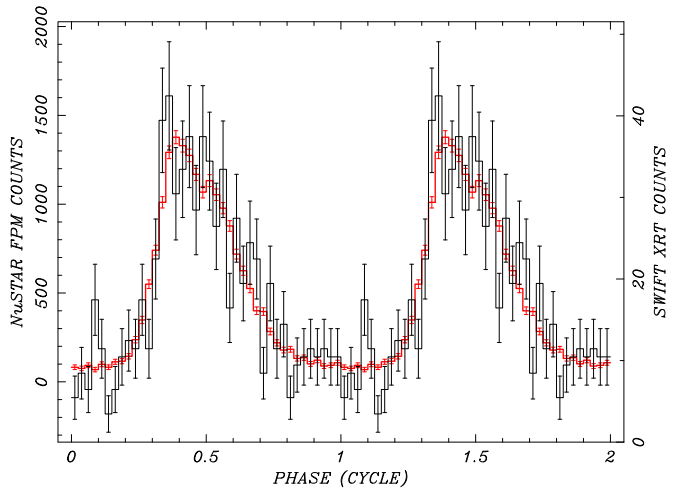

Figure 10. *NuSTAR* (red line) and *Swift* (black line) pulse profile of PSR B1509−58 in the overlapping 3–10 keV energy band folded in 40 phase bins on the same ephemeris. The data were acquired nearly simultaneously in time. The calculated phase lag between the two profiles is less than one phase bin. Two cycles are displayed for clarity.

(A color version of this figure is available in the online journal.)

data, and no published ephemeris is available for that epoch, we generated a *Fermi* ephemeris that covers the end of the *XMM-Newton* observations to the *NuSTAR* data. In the following, photon arrival times from all Geminga data sets were corrected to the solar system barycenter using the JPL D200 ephemeris calculated using the *HST* coordinates of Caraveo et al. (1998) and the proper motion of Faherty et al. (2007), updated from Caraveo et al. (1996), reproduced in Table 3.

Table 1 lists all archival *XMM-Newton* observations for Geminga acquired in high time-resolution `SmallWindow` mode. Observational details for these data sets are presented in Section 3. For our timing analysis we selected 0.2–10 keV source photons from a 30″ radius aperture centered on Geminga. Extracted data were initially folded at the period for the peak signal using the Z_1^2 statistic and cross-correlated with an iterated high statistic pulse profile to generate times-of-arrival (TOAs) for each data set. These TOAs were fitted to a phase model with two frequency derivatives initiated using the overlapping EGRET ephemeris. This process was iterated to produce the *XMM-Newton* ephemeris presented in Table 3.

To overlap with the *XMM-Newton* ephemeris, we analyzed *Fermi* data covering the mission start to the *NuSTAR* epoch. Data were obtained from the *Fermi*/Large Area Telescope archive and photons selected from the 200 MeV to 10 GeV range within a 1.°3 aperture centered on the pulsar. These photons were filtered to include only events tagged as `Pass 7` "Source" photons and restricted to a maximum zenith angle of $\phi < 100°$. *Fermi* photon arrival times were binned into 20 day intervals and folded on the *XMM-Newton* ephemeris to generate TOAs as described above. These TOAs were fitted to produce an iterative *Fermi* ephemeris presented in Table 3.

APPENDIX B

PRELIMINARY LIMITS ON THE ABSOLUTE TIMING ACCURACY WITH *NuSTAR*

The *NuSTAR* photon arrival times are corrected for spacecraft clock drift with a typical rms residual uncertainty of ∼2 ms, dominated by orbital temperature variations of the clock. A high-resolution *NuSTAR* absolute timing calibration is underway using Crab observations to attempt to reduce these variations. For the present study, we verify that the *NuSTAR* timestamps are of sufficient accuracy, in absolute TDB time, to co-add phase-resolved *NuSTAR* Geminga spectra with those obtained with the *XMM-Newton* mission. For this purpose we have analyzed near simultaneous *Swift* and *NuSTAR* observations of the 151 ms pulsar B1509−58 in supernova remnant MSH 15−52. Any time offset is already known to be less than 151 ms from comparisons of *Swift* and *NuSTAR* observations of the 3.79 s pulsar SRG J1745−2900 (Mori et al. 2013; Kaspi et al. 2014).

A *NuSTAR* observation of PSR B1509−58 (ObsID 40024004002) was obtained on 2013 June 7 to study the PWN MSH 15−52. The default pipeline processing resulted in a total of 45 ks of good data. A short, 2.8 ks *Swift* X-Ray Telescope observation (ObsID 00080517001) was acquired 105 s prior to the end of the *NuSTAR* observation. The default *Swift* pipeline was run on the two consecutive orbits of data (7340 s span) taken in window timing mode. This mode provides 1.78 ms timestamps with clock-drift corrected MJD absolute TDB *Swift* times better than 0.2 ms (Cusumano et al. 2012). For this study it is not necessary to apply the UVOT attitude correction to try and improve the *Swift* absolute time accuracy. Both data sets were barycentered using the JPL DE200 solar system ephemeris and the *Chandra* (ObsID 3833) determined coordinates (J2000) $15^h13^m55^s.66$, $-59°08'09''.2$ (epoch MJD 52930).

The *NuSTAR* and *Swift* observations yield a total of 22, 629, and 796 counts, respectively, extracted from an aperture of $r = 0'.5$ radius in the overlapping 3–10 keV energy band. Figure 10 compares the pulse profile from the two missions folded on the same period and period derivative at epoch MJD 56450.885504116, in 40 phase bins. The period was determined from the peak signal in the highly significant *NuSTAR* data set using the Z_5^2 statistic and the period derivative was obtained from the radio ephemeris reported in Martin-Carrillo et al. (2012). Cross-correlating the two profiles yields a phase lag corresponding to a relative time offset of $\Delta\phi = 1.0 \pm 2.0$ ms, comparable with the residual uncertainty in the *NuSTAR* clock drift correction. This measurement represents an upper limit since the (1σ) error is dominated by the photon counts of the short *Swift* exposure. We conclude that the present data are consistent with the result of no measurable phase offset compared to the calibrated *Swift* clock. This verifies that the *NuSTAR* absolute time is sufficiently accurate to phase align co-added *XMM-Newton* and *NuSTAR* spectral data for Geminga in 10 phase bins.

REFERENCES

Abdo, A. A., Ackermann, M., Ajello, M., et al. 2010, ApJ, 720, 272
Alexander, D. M., Stern, D., Del Moro, A., et al. 2013, ApJ, 773, 125
Bertsch, D. L., Brazier, K. T. S., Fichtel, C. E., et al. 1992, Natur, 357, 306
Bignami, G. F., & Caraveo, P. A. 1992, Natur, 357, 287
Bignami, G. F., & Caraveo, P. A. 1996, ARA&A, 34, 331
Bignami, G. F., Caraveo, P. A., & Mereghetti, S. 1993, Natur, 361, 704
Caraveo, P. A. 2014, ARA&A, 52, 211
Caraveo, P. A., Bignami, G. F., De Luca, A., et al. 2003, Sci, 301, 1345
Caraveo, P. A., Bignami, G. F., Mignani, R., & Taff, L. G. 1996, ApJL, 461, L91
Caraveo, P. A., De Luca, A., Mereghetti, S., Pellizzoni, A., & Bignami, G. F. 2004, Sci, 305, 376
Caraveo, P. A., Lattanzi, M. G., Massone, G., et al. 1998, A&A, 329, L1
Cheng, K. S., Ho, C., & Ruderman, M. 1986, ApJ, 300, 522
Cheng, K. S., & Zhang, L. 1999, ApJ, 515, 337
Cusumano, G., La Parola, V., Capalbi, M., et al. 2012, A&A, 548, A28

Danilenko, A. A., Zyuzin, D. A., Shibanov, Y. A., & Zharikov, S. V. 2011, MNRAS, 415, 867
de Luca, A., Caraveo, P. A., Mattana, F., Pellizzoni, A., & Bignami, G. F. 2006, A&A, 445, L9
De Luca, A., Caraveo, P. A., Mereghetti, S., Negroni, M., & Bignami, G. F. 2005, ApJ, 623, 1051
Durant, M., Kargaltsev, O., & Pavlov, G. G. 2011, ApJ, 743, 38
Faherty, J., Walter, F. M., & Anderson, J. 2007, Ap&SS, 308, 225
Greenstein, G., & Hartke, G. J. 1983, ApJ, 271, 283
Halpern, J. P., & Holt, S. S. 1992, Natur, 357, 222
Halpern, J. P., & Ruderman, M. 1993, ApJ, 415, 286
Halpern, J. P., & Wang, F. Y.-H. 1997, ApJ, 477, 905
Harding, A. K., Stern, J. V., Dyks, J., & Frackowiak, M. 2008, ApJ, 680, 1378
Harding, A. K., Strickman, M. S., Gwinn, C., et al. 2002, ApJ, 576, 376
Harrison, F. A., Craig, W. W., Christensen, F. E., et al. 2013, ApJ, 770, 103
Jackson, M. S., & Halpern, J. P. 2005, ApJ, 633, 1114
Jackson, M. S., Halpern, J. P., Gotthelf, E. V., & Mattox, J. R. 2002, ApJ, 578, 935
Kargaltsev, O. Y., Pavlov, G. G., Zavlin, V. E., & Romani, R. W. 2005, ApJ, 625, 307
Kaspi, V. M., Archibald, R. F., Bhalerao, V., et al. 2014, ApJ, 786, 84
Lattimer, J. M., & Prakash, M. 2007, PhR, 442, 109
Lyutikov, M. 2013, MNRAS, 431, 2580
Martin-Carrillo, A., Kirsch, M. G. F., Caballero, I., et al. 2012, A&A, 545, A126
Mori, K., Gotthelf, E. V., Zhang, S., et al. 2013, ApJL, 770, L23
Nynka, M., Hailey, C. J., Mori, K., et al. 2013, ApJL, 778, L31
Pavlov, G. G., Bhattacharyya, S., & Zavlin, V. E. 2010, ApJ, 715, 66
Pavlov, G. G., Sanwal, D., & Zavlin, V. E. 2006, ApJ, 643, 1146
Pavlov, G. G., Shibanov, Y. A., Zavlin, V. E., & Meyer, R. D. 1995, in Proc. NATO Advanced Study Institute, The Lives of the Neutron Stars, ed. M. A. Alpar, U. Kiziloglu, & J. van Paradijs (Dordrecht: Kluwer), 71
Pavlov, G. G., Zavlin, V. E., Truemper, J., & Neuhaeuser, R. 1996, ApJL, 472, L33
Romani, R. W. 1996, ApJ, 470, 469
Romani, R. W., & Yadigaroglu, I.-A. 1995, ApJ, 438, 314
Shibanov, Y. A., Zharikov, S. V., Komarova, V. N., et al. 2006, A&A, 448, 313
Thompson, D. J., Fichtel, C. E., Hartman, R. C., Kniffen, D. A., & Lamb, R. C. 1977, ApJ, 213, 252
Verner, D. A., Ferland, G. J., Korista, K. T., & Yakovlev, D. G. 1996, ApJ, 465, 487
Wang, F. Y.-H., Ruderman, M., Halpern, J. P., & Zhu, T. 1998, ApJ, 498, 373
Wilms, J., Allen, A., & McCray, R. 2000, ApJ, 542, 914